processes

MDPI

Article

Insight into the Crack Evolution Characteristics Around the Ridged PDC Cutter During Rock Breaking Based on the Finite–Discrete Element Method

Jianxun Liu [1,2,*], Taixue Hu [1], Xikun Ma [1], Chengbin Mei [1] and Chaoqun Dong [1]

[1] School of Mechanical and Intelligent Manufacturing, Chongqing University of Science & Technology, Chongqing 401331, China; 2025204018@cqust.edu.cn (T.H.); 2025204057@cqust.edu.cn (X.M.); 2025204079@cqust.edu.cn (C.M.); 2015004@cqust.edu.cn (C.D.)
[2] Key Laboratory of Oil and Gas Equipment, Ministry of Education, Chengdu 610500, China
* Correspondence: 2020043@cqust.edu.cn

Abstract

The ridged cutter, a highly representative non-planar PDC cutter known for its strong impact resistance and wear durability, has demonstrated significant effectiveness in enhancing the rate of penetration (ROP) in hard, highly abrasive, and interbedded soft–hard formations. Understanding the crack evolution is fundamental to revealing the rock-breaking mechanism of ridged PDC cutters. To date, studies on rock breaking with ridged cutters have largely focused on macroscopic experimental observations, lacking an in-depth understanding of the crack evolution characteristics during the rock fragmentation process. This study employs the Finite–Discrete Element Method (FDEM) to establish a three-dimensional numerical model for simulating the interaction between the ridged cutter and the rock. By analyzing crack propagation paths, stress distribution, and the stiffness degradation factor (SDEG), the initiation, propagation patterns, and sequence of cracks around the cutter are investigated. The results indicate the following outcomes: (1) The ridged cutter breaks rock mainly by tensioning and shearing, while the conventional planar cutter breaks the rock by shearing. (2) The rock-breaking process proceeds in three stages: compaction, micro-failure, and volumetric fragmentation. (3) Crack evolution around the cutter follows the rule of "tension-initiated and shear-propagation"; that is, tensile damage first generates at the front of the crack due to tensile stress concentration, whereas shear damage subsequently occurs at the rear under high shear stress. Finally, mixed tensile–shear macro-cracks are generated. (4) The spatial distribution of cracks exhibits strong regional heterogeneity. The zone ahead of the cutter contains mixed tensile–shear cracks, forming upward-concave cracks, horizontal cracks, and oblique cracks at 45°. The sub-cutter zone is dominated by tensile cracks; the zone on the flank side of the cutter consists of a radial stress field, accompanied by oblique 45° cracks. The synergistic evolution mechanism and distribution law of tensile–shear cracks revealed in this study elucidate the rock-breaking advantages of ridged cutters from a micro-crack perspective and provide a theoretical basis for optimizing non-planar cutter structures to achieve more efficient volumetric fracture.

Keywords: ridged cutter; Finite–Discrete Element Method (FDEM); peri-cutter zone; crack evolution; tensile–shear failure

check for updates

Academic Editor: Dan Zhang

Received: 22 August 2025
Revised: 15 September 2025
Accepted: 18 September 2025
Published: 23 September 2025

Citation: Liu, J.; Hu, T.; Ma, X.; Mei, C.; Dong, C. Insight into the Crack Evolution Characteristics Around the Ridged PDC Cutter During Rock Breaking Based on the Finite–Discrete Element Method. *Processes* **2025**, *13*, 3039. https://doi.org/10.3390/pr13103039

Copyright: © 2025 by the authors. Licensee MDPI, Basel, Switzerland. This article is an open access article distributed under the terms and conditions of the Creative Commons Attribution (CC BY) license (https://creativecommons.org/licenses/by/4.0/).

1. Introduction

Polycrystalline Diamond Compact (PDC) bits are widely used for forming oil and gas channels due to their excellent rock-breaking performance. Although the conventional PDC cutter performs well in shallow formations, it exhibits low efficiency and a short service life in deeper formations owing to the planar geometry. With improvements in diamond-manufacturing technology [1–3], various kinds of non-planar cutters have emerged (see Figure 1). In 2010, Smith Bits developed the ridged cutter. Subsequently, numerous scholars and companies proposed various non-planar cutters, such as tri-plane, 3-ridged, V-shaped, and concave cutters. Among those, the ridged cutter, being one of the earliest designs, has been the most widely adopted and has achieved excellent field performance. However, due to the spatial three-dimensional structure of its diamond layer, the rock-breaking mechanism and layout parameters of the ridged cutter are quite different from those of conventional planar cutters. Moreover, research on the crack-evolution characteristics around the ridged cutter remains unclear.

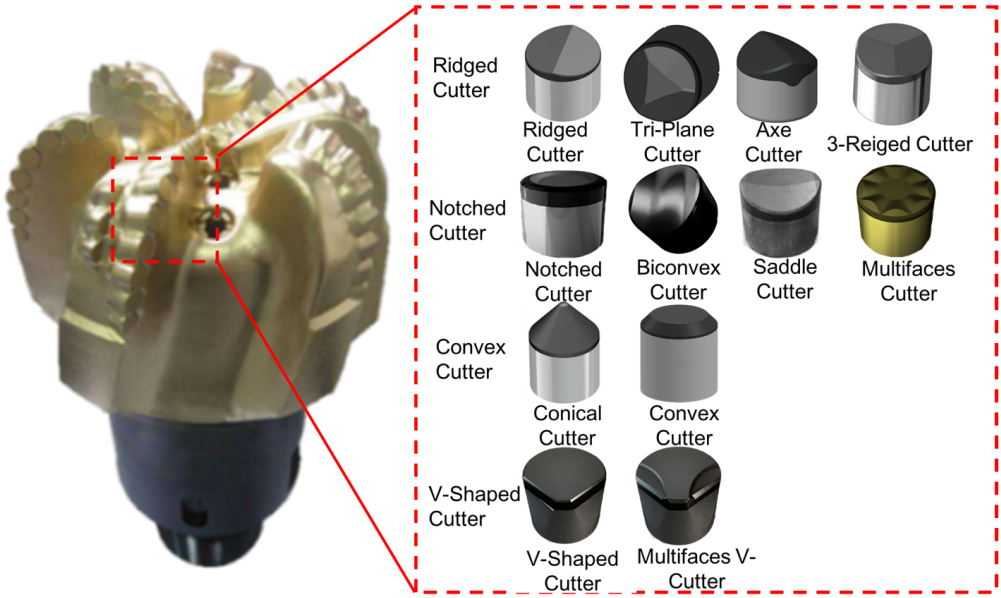


Figure 1. PDC bit and non-planar PDC cutters.

In recent years, many scholars have conducted extensive research on the above issues. Taking the ridged cutter as an example, researchers have employed physical experiments and numerical simulations to investigate the macro rock-breaking characteristics, breaking laws, optimization of cutting parameters, as well as impact and abrasion resistance, yielding abundant results. From the experimental perspective, Zou et al. [4] found that the tangential and axial forces of ridged cutters are lower than those of planar cutters under the identical condition, and the fluctuation amplitude of cutting load is also smaller. This indicates that ridged cutters penetrate rock more easily, more aggressively, and more stably. Xu et al. [5] designed a single cutter-rock breaking test to study the efficiency of conical cutters breaking complex formations. Results show that when the forward rake angle of conical cutters is 20°, the cutters exhibit higher stability and the bit vibration intensity is minimal. Huang's team [6,7] employed a 3D profilometer to quantify the surface topography of rock penetrated by conical and planar cutters, along with the cutting groove morphology and debris characteristics. Their work determined the optimal attack angle and revealed the mechanical mechanism: conical cutters achieve efficient rock breaking through a strong point load at the tip, combined with tensile stresses generated around the cutter. Shao et al. [8] compared the differences in cutting load and thermal stability when

ridged and planar cutters penetrated into the rock by a vertical turret lathe. They evaluated the ability of anti-wear and impact resistance abilities using 3D optical profilometry.

From the perspective of numerical research, Zhang [9] employed the Discrete Element Method (DEM) to explore the crack propagation when the planar cutter breaks the rock. Yao et al. [10] considered the influence of temperature and in situ stress and built DEM models to investigate rock failure characteristics for the planar cutters, 3-ridged, ridged, and V-shaped cutters. They found that the 3-ridged cutter achieved the highest rock-breaking efficiency under different cutting parameters. Kuang et al. [11], Gao et al. [12], Zhu et al. [13], and others used ABAQUS 6.14 with the Drucker–Prager (DP) or Mohr–Coulomb (MC) model and shear damage criterion, as well as the erosion algorithm, to study dynamic rock breaking by planar cutters. They revealed the shear rock-breaking mechanism of planar cutters, as well as the influence of the forward rake angle, side rake angle, and cutting speed on breaking efficiency. Liu [14] also adopted this method to investigate the rock-breaking mechanism of 3-ridged and planar cutters and elucidated their differences and evaluated their efficiencies. Chen et al. [15] used the finite element method (FEM) to establish numerical models of planar, ridged, and 3-ridged cutters breaking plastic mudstone. Results show that ridged cutters exhibit higher efficiency than 3-ridged cutters. Shao et al. [16] compared the differences in single- and multi-ridged cutters using the JH-2 constitutive model. They found that multi-ridged cutters require smaller cutting forces and possess better impact and wear resistance under identical conditions.

Currently, analysis of rock breaking by cutters mainly uses two methods: discrete and continuum approaches. Discrete methods, represented by software like PFC 6.0, can effectively simulate crack formation and propagation. However, these methods are not well-suitable for large-scale models. Continuum methods, such as those modeled using erosion algorithms, simulate cracks through element deletion. While somewhat effective, the deletion of elements leads to non-conservation of mass and abnormal energy loss. This reduces the reliability of simulations. This is especially true with large mesh sizes or high fragmentation levels, where results become highly inaccurate. Due to these limitations, researchers have used a combined continuum–discontinuum method, that is, the finite-discrete element models (FDEM) for rock cutting. Based on this approach, many studies have been carried out. Qin et al. [17] used an FDEM model to simulate the process of rock breaking with a planar cutter under combined impact. Based on the debris and cracks, they revealed rock failure patterns and found the method captures crack initiation, propagation, coalescence, and contact between fragments. Liu et al. [18] used FDEM to analyze the rock-breaking mechanism in deep surrounding rock under mechanical impact. They investigated the effect of confining pressure and micro-mechanical parameters on rock failure. Wu et al. [19] employed FDEM, coupled with the arbitrary Lagrangian–Eulerian (ALE) method, to study the dynamic failure process of concrete under explosive loading. Feng et al. [20] simulated a three-dimensional bench blasting in an open-pit mine using FDEM. They found that the method can describe rock damage, crack development, and fragment collision, movement, and accumulation.

In summary, existing research on non-planar cutters mainly focuses on the macroscopic mechanical responses (e.g., cutting force and specific energy) and fragmentation effects, whereas the key microscopic physical mechanisms—namely the initiation sequence, propagation types, and spatial evolution of cracks around cutters—remain insufficiently studied. Therefore, this paper establishes a ridged cutter-rock breaking model using the FDEM and analyzes the crack patterns as well as characteristics around the cutter from the perspective of rock damage and crack evolution. The results can provide a theoretical basis for optimizing a non-planar cutter's structure to achieve more efficient volumetric fracture.

2. Basic Principle of the FDEM

Rock can be treated as a combination of continuous and discontinuous media. The FDEM, proposed by Munjiza [21], can better simulate the rock failure process [22]. It combines the advantages of continuous and discontinuous approaches and is widely used to simulate material or structural fracture. In the FDEM, before the fracture, the stress–strain response of the rock bulk is modeled by the Drucker–Prager (DP) plasticity criterion. Fracture, including crack initiation and propagation, is simulated by the softening and failure of discrete elements once their strength limits are exceeded.

2.1. Rock Constitutive Model

Under external influences, rock exhibits complex stress-deformation and failure behaviors, which cannot be adequately described using constitutive models designed for metallic materials. The DP criterion combines the features of the Mohr–Coulomb (MC) and von Mises criteria. It not only accounts for the influence of intermediate principal stress but also incorporates a hydrostatic pressure term. This enables a more comprehensive characterization of rock strength properties. The criterion effectively captures the elastoplastic behavior of rocks prior to peak strength, particularly capturing hydrostatic pressure dependence and shear failure mechanisms. It also accurately reflects the dilatancy effect that occurs in rocks after exceeding their strength limit. These characteristics give it distinct advantages in simulating plastic failure behavior of rock-like materials, leading to its widespread application in rock-breaking studies [23]. Consequently, this study adopts the DP criterion for the rock, expressed as

$$q = p \tan \beta + d \tag{1}$$

where p is the average stress, q is the equivalent stress, and tan β, d are determined by the cohesion and friction angle.

2.2. Discrete Elements Constitutive Model

The rock is discretized into continuum elements with an embedded network of zero-thickness discrete elements inserted between all bulk element faces [24]. The discrete element obeys the traction–separation law, which assumes that the element initially exhibits a linear elastic behavior, then experiences damage initiation and evolution until it fails. The failure of discrete elements is used to reproduce crack initiation, propagation, and coalescence.

As shown in Figure 2, in the linear elastic stage, the relationship between stress and displacement is

$$\mathbf{t} = \begin{Bmatrix} t_{\mathrm{n}} \\ t_{\mathrm{s}} \\ t_{\mathrm{t}} \end{Bmatrix} = \mathbf{K} \cdot \varepsilon = \begin{bmatrix} K_{\mathrm{nn}} & K_{\mathrm{ns}} & K_{\mathrm{nt}} \\ K_{\mathrm{ns}} & K_{\mathrm{ss}} & K_{\mathrm{st}} \\ K_{\mathrm{nt}} & K_{\mathrm{st}} & K_{\mathrm{tt}} \end{bmatrix} \cdot \begin{Bmatrix} \varepsilon_{\mathrm{n}} \\ \varepsilon_{\mathrm{t}} \\ \varepsilon_{\mathrm{s}} \end{Bmatrix} \tag{2}$$

where $\boldsymbol{t}$ and $\boldsymbol{\varepsilon}$ are the nominal traction stress and strain vector, respectively; $\mathbf{K}$ is the stiffness matrix; t_n, t_s, and t_t are the nominal traction stress in the normal and two tangential directions, respectively; δ_n, δ_s, and δ_t are the corresponding displacement; ε_n, ε_s, and ε_t are the corresponding strain.

When there is no damage in discrete element (i.e., D = 0), the traction in each direction increases linearly with the relative displacement. This paper assumes that there is no coupling between t_n, t_s, and t_t, and adopts the maximum nominal stress criterion (expressed

by Equation (3)) to determine whether the discrete element enters the damage evolution stage [24,25]:

$$\max\left\{\frac{t_n}{t_n^0}, \frac{t_s}{t_s^0}, \frac{t_t}{t_t^0}\right\} = 1 \tag{3}$$

where t_n^0, t_s^0 and t_t^0 denote the nominal stresses in the normal and tangential directions when the damage begins. Therefore, once the stress of discrete elements reaches any of t_n^0, t_s^0 and t_t^0, which means the damage-initiation criterion is met, the discrete element then begins to damage. At this time, the stiffness degradation factor (SDEG) equals to zero. As the displacement gradually increases further, the stress begins to decrease, and the load-bearing capacity correspondingly decreases. The crack gradually starts to propagate, and the SDEG value increases simultaneously. During the entire process, the stress in each direction can be calculated as

$$t_n = \begin{cases} (1-D){t_n}^0, {t_n}^0 \geq 0 \\ {t_n}^0, {t_n}^0 \leq 0 \end{cases} \tag{4}$$

$$\begin{cases} t_s = (1-D){t_s}^0 \\ t_t = (1-D){t_t}^0 \end{cases} \tag{5}$$

where D is the damage variable.

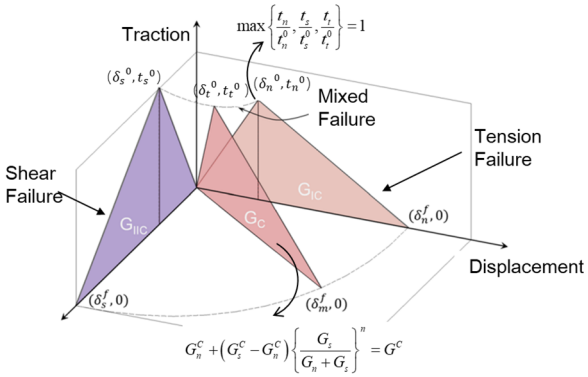


Figure 2. Traction separation mechanism theorem.

The effective displacement δ_m is used to characterize the damage evolution of the discrete element under the combination of normal and shear deformation

$$\delta_m = \sqrt{{\delta_n}^2 + \delta_s^2 + \delta_t^2} \tag{6}$$

The damage variable D can be defined as

$$D = \frac{\delta_m^f\left(\delta_m^{\max} - \delta_m^0\right)}{\delta_m^{\max}\left(\delta_m^f - \delta_m^0\right)} \tag{7}$$

where δ_m^{max} is the maximum effective displacement during loading, δ_m^0 is the effective displacement on the set of damage initiation, and δ_m^f is the effective displacement when the element completely fails.

When the stress decreases to zero, the discrete element reaches its ultimate allowable displacement. This ultimate displacement is termed the crack opening displacement or failure displacement. At this stage, the crack is fully propagated, and the fracture surface fails at that location. With a continued increase in displacement, the interfacial gap widens, and the crack becomes broader. This process is then transferred to the next discrete element,

and the cycle repeats. This leads to a progressively longer and wider fracture surface, resulting in a crack that grows both in length and width. ABAQUS can identify whether an element has failed and assess the extent of damage by outputting SDEG. It should be pointed out that in the FDEM model, the sudden deletion of cohesive elements (SDEG ≥ 1) may cause convergence difficulties, so the SDEG threshold is adjusted to 0.9 [26–29]. This indicates that when the SDEG reaches 0.9, the discrete element is considered fully failed in the mechanical sense. It can no longer transfer loads effectively but remains in the model.

The Benzeggagh–Kenane (BK) criterion allows for more precise handling of mixed-mode damage scenarios where multiple types of damage (e.g., Mode-I tension failure and Mode-II shear failure) coexist, thereby enabling a more realistic simulation of material damage behavior under complex loading conditions. Numerous studies [30–33] have demonstrated that the BK criterion exhibits good agreement with experimentally measured data, such as fracture energy and damage propagation paths, when simulating mixed-mode damage in real materials. Therefore, this paper adopts the BK criterion to describe the damage evolution of cohesive elements:

$$G_n^C + \left(G_s^C - G_n^C\right)\left\{\frac{G_s}{G_n + G_s}\right\}^n = G^C \tag{8}$$

where G is the total fracture energy, corresponding the area of the triangle in Figure 2, G_n^C and G_S^C are the mode-I and mode-II fracture energies, respectively. G_n and G_s are the work performed by the traction force in normal and tangential directions, respectively.

3. Numerical Modeling

3.1. Geometry Model

The following assumptions are adopted for the ridged cutter-rock-breaking simulation: (1) the cutting process is simplified to linear cutting [24]; (2) rock is treated as a homogeneous, isotropic material, and the effects of confining pressure, drilling fluid, and temperature are neglected; and (3) the ridged cutter is assumed rigid.

The ridged cutter-rock-breaking model is built in ABAQUS 6.14. According to Saint-Venant's principle, the rock specimen measures 20 mm × 60 mm × 35 mm to avoid boundary effects. The ridge height is 2.0 mm, and the ridge length is 7.5 mm (see Figure 3). For the cutter, the diameter is 15.88 mm and the ridge angle is 153.2°. The cutting depth is 1.6 mm, and the forward rake angle is 10°. The cutter is constrained against rotation about the X and Y axes, ensuring that its ridge remains perpendicular to the rock surface.

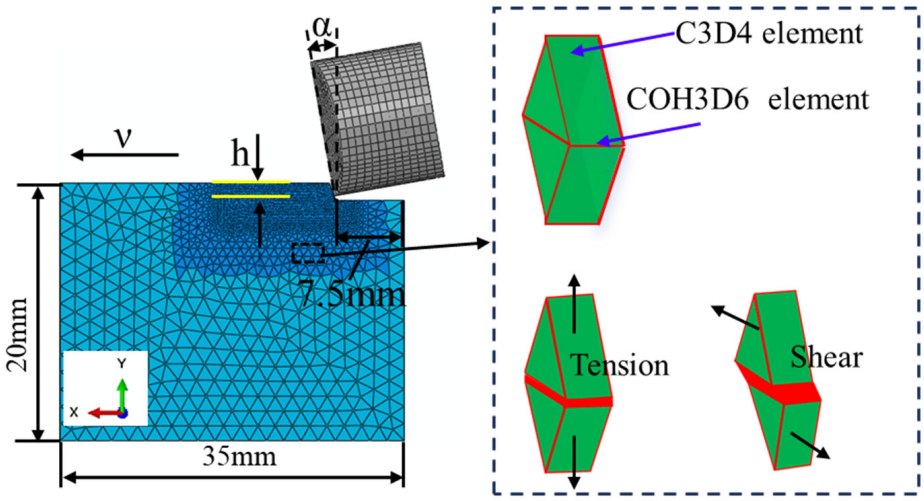


Figure 3. FDEM model of the ridged cutter-rock breaking.

3.2. Mesh and Boundary Conditions

In order to balance the calculation time and the simulation accuracy, the potential crack-propagation zone around the cutter (10 mm × 20 mm × 5 mm) is mesh-refined. The element size is set to 0.4 mm in this zone [24], and cohesive elements are inserted between the rock bulk elements. The remainder is meshed from 0.4 mm to 2.0 mm. Given the ridged cutter's strength is much higher than that of the rock, the ridged cutter is regarded as a discrete rigid body to ensure computational accuracy and efficiency. It is discretized using a structured hexahedral mesh with 8-node reduced integration elements (C3D8R). The mesh size is 1 mm, with a total of 3510 nodes. After generating the rock elements, the nodes and elements information can be extracted. As shown in Figure 4, specific nodes in the cutter-rock interaction region are duplicated and renumbered based on the number of shared node elements. Zero-thickness cohesive elements (COH3D6) are then inserted at the interfaces using the coordinates of the renumbered nodes, with a total of 240,365 nodes.

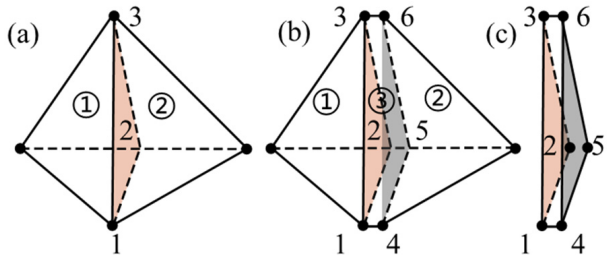


Figure 4. Embedding a wedge-shaped cohesive element in a tetrahedron: (**a**) two adjacent tetrahedral elements; (**b**) embedding a 3D cohesive element; and (**c**) a six-node wedge cohesive element.

In the process of rock breaking, there is highly nonlinear dynamic behavior with large deformation. The cutter–rock interface undergoes continuous dynamic contact. Thus, the explicit dynamic algorithm is used to monitor the contact status. Considering the possible interaction during debris splashing, the general contact is chosen, and hard contact allows separation. The friction coefficient between the cutter and rock was set to 0.4 [34,35], which is a representative value for diamond–rock interfaces widely used in numerical studies.

For the rock, the top surface is set to be free, and the remaining surfaces are fixed. The cutter moves at 0.3 m/s along the X axis, while the other five degrees of freedom are constrained. To more accurately simulate the debris splashing phenomenon during rock breaking, the gravity acceleration is applied in the negative direction of the Y axis. During the simulation, the ridge tooth is regarded as a rigid body without considering its deformation. The macroscopic rock mechanical parameters and the microscopic cohesive interface parameters were adopted from a systematic study on Nanchong sandstone in the literature [24]. That study employed an iterative calibration process (i.e., a 'trial-and-error' method) by comparing the numerical results of Brazilian splitting and uniaxial compression tests with physical experimental data, ultimately determining a parameter set that accurately reproduces the crack propagation behavior of Nanchong sandstone. Specific parameter values are listed in Table 1.

Table 1. Parameters of the rock.

Parameters	Value
Density (kg/m^3)	2230
Young's modulus (GPa)	4.049
Poisson's ratio	0.3
Compressive strength (MPa)	25.54
Tensile strength (MPa)	1.631
Shear strength (MPa)	7.0

Table 1. *Cont.*

Parameters	Value
Friction angle (°)	27
Cohesion (MPa)	7.0
Normal stiffness (N/mm)	125
Shear stiffness (N/mm)	62.5
Mode-I fracture energies G_I (N/mm^2)	0.02
Mode-II fracture energies G_{II} (N/mm^2)	0.25

4. Results

4.1. Fragmentation Process Analysis

The macroscopic rock-breaking process is the direct manifestation of the development of internal cracks and is the basis of understanding the evolution law of rock cracks. Figure 5 shows the process of rock breaking within 0–19 ms. It can be seen that the crushing process is as follows: (1) When the cutter contacts the rock, the rock is squeezed. Then the micro-cracks sprout; (2) With the continuous movement of the cutter, the zone of the rock, which is located around the cutter, forms a compaction core, and the micro-cracks propagate; (3) As the load between the cutter and the rock gradually increases, the compaction core area further expands, and the cracks around the cutter propagate, intersect, and coalesce. The increasing load causes the volumetric fragmentation of the rock, and the debris gradually separates from the rock. The generated debris mainly consists of two types: fine fragments and block-shaped fragments, with the latter being less than the former; (4) The fine fragments detach from the rock and splatter in all directions, while the larger fragments travel essentially parallel to the motion of the cutter. Finally, the fragments are completely separated from the rock.

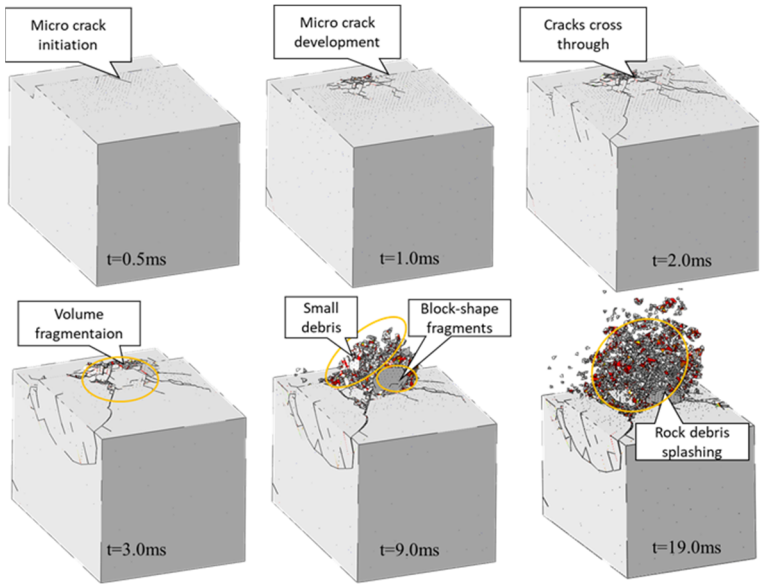


Figure 5. The process of rock-breaking under the action of a ridged cutter.

In summary, the rock-breaking process can be divided into three stages: compaction, micro-damage, and volumetric fragmentation. The resulting damage and failure morphologies exhibit markedly regional characteristics, which can be classified as (1) the fracture zone (volumetric fragmentation zone), (2) the damage-deformation zone (crack-propagation zone), and (3) the plastic-extension zone (crack-free zone).

4.2. Analysis of Cracks Ahead of the Cutter

After identifying the rock fracture process, this section will further systematically investigate the above process from the perspective of crack evolution. In order to describe the spatial distribution of the cracks around the cutter, two cross-sections—denoted A and B—are defined, as illustrated in Figure 6. Section A is positioned at the symmetry plane of the model in the Z-direction, while Section B is situated 1.6 mm below the upper surface of the rock.

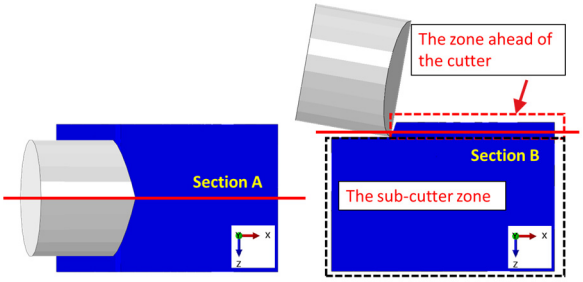


Figure 6. Schematic diagram of slice locations.

Figure 7 presents the evolution of cracks, maximum principal stress, and shear stress in the longitudinal profile of the rock within the time range of 0.3 ms to 3.0 ms. As it is shown in the figure, the ridged cutter contacts the rock at 0.3 ms. Due to the cutter's extrusion, a distinct compressive zone appears at the cutter-rock interface (Figure 7e), resulting in a compaction core. The stress area is relatively small and primarily distributed around the cutter-rock contact region. With the continuous movement of the cutter, crack A initiates from the compaction core and propagates at an angle of approximately 45° (Figure 7b), which extends toward the free surface at the top of the rock. The area near the origin of crack A experiences a mixed tensile–shear stress state (Figure 7f,j). Note that the positive value of maximum main stress indicates tensile stress, while negative values present compressive stress.

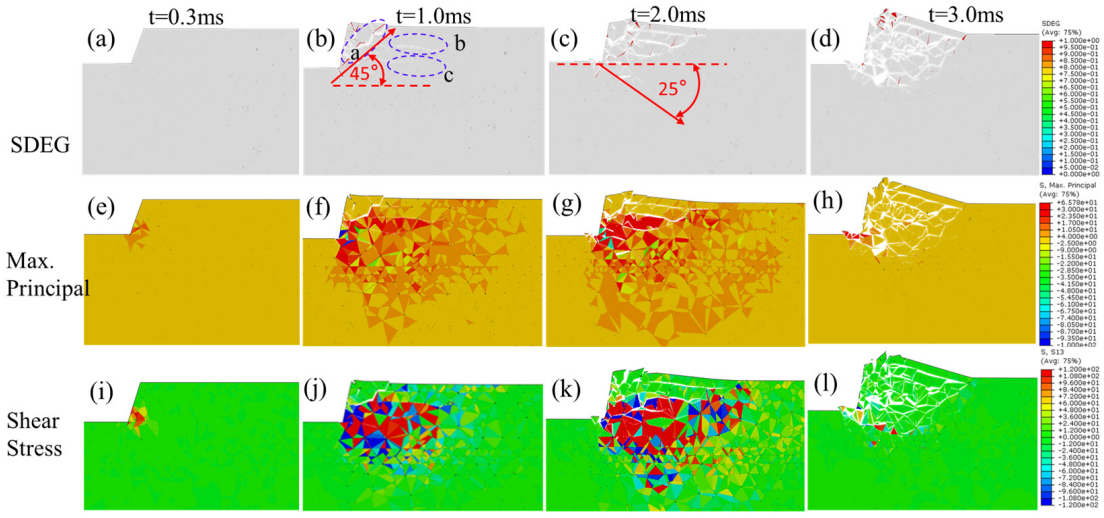


Figure 7. Characteristics of cracks on the longitudinal profile of the rock (Section A).

In addition to the region near the cutter, there are also two parallel micro-cracks, b and c, in the region ahead of the cutter. These cracks are accompanied by distinct tensile stress bands and extend to the top free surface (Figure 7f,g). Meanwhile, the shear–stress nephogram also reveals a corresponding shear region, ahead of the cutter, extending to the free surface (Figure 7j,k). As the cutter continues to move forward, the cracks gradually

propagate and develop into an upward-concave crack, leading to the rock spalling off as a block and the occurrence of volumetric fragmentation (Figure 7d,h,l).

As shown in Figure 8a, six cohesive elements labeled A1 to A6 are selected along the upward-concave crack. Their SDEG values at 2.0 ms are extracted, as listed in Table 2. It can be observed that the normal SDEG of elements A1–A3 is significantly higher than that of the tangential SDEG, but none of them reach the critical threshold of 0.9. This indicates that the elements at these locations are in a tensile-dominated crack initiation stage, whereas the shear damage has not yet become dominant. However, the SDEG of elements A4–A6 in all directions has reached 0.9, indicating that these elements have completely failed. It means that the crack has fully propagated, and the failure mode is a tensile–shear mix. Overall, the damage distribution along the crack path shows a pattern that the damage is relatively milder at the front end and more severe at the rear end. It can be observed from Figure 8b that there is splashing debris in the region ahead of the cutter. Cracks initiate from the cutter tip and propagate along the cutting direction, eventually extending to the free surface and forming larger fragments. The numerical results agree well with those of experiments in Reference [26].

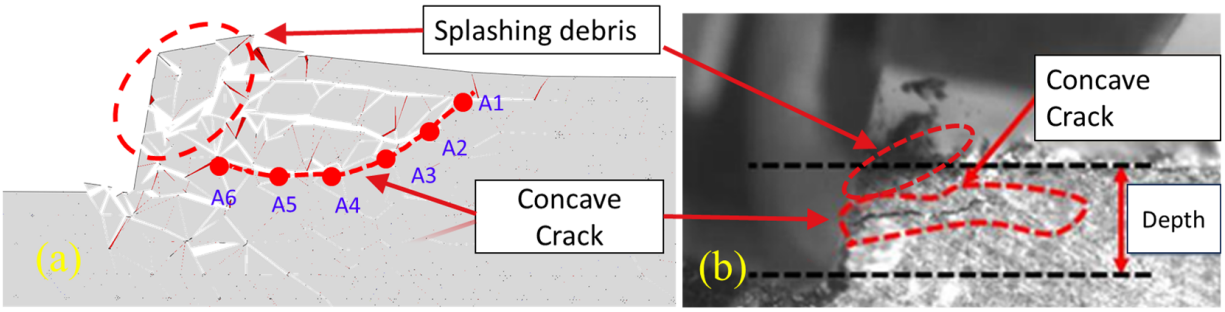


Figure 8. Comparison of rock fragmentation ahead of the cutter: (**a**) Figure 7c in this paper, (**b**) experimental picture [26].

Table 2. SDEG values of cohesive elements along the macro-crack.

Location	Element Number	SDEG (n.s.t)
A1	177,000	**(0.81,** 0.74, 0.73**)**
A2	129,858	**(0.83,** 0.79, 0.79**)**
A3	131,456	**(0.87,** 0.76,0.78**)**
A4	179,636	**(0.90, 0.90, 0.90)**
A5	93,987	**(0.90, 0.90, 0.90)**
A6	111,701	**(0.90, 0.90, 0.90)**

The reason is likely that the rock at the front end of the crack (A1–A3) is far from the ridged cutter and less affected by its extrusion. The stress state in this region is dominated by the tensile stress, with relatively low shear stress (see Figure 7f,j). Since the tensile strength of rock is much lower than its shear strength, the front-end rock is more prone to tensile damage, being "pulled apart" to form tensile cracks. On the other hand, the rock at the rear end of the crack (A4–A6) is located in a mixed tensile–shear stress zone (see the overlapping area of the red zone in Figure 7f and the yellow zone in Figure 7j) and is closer to the cutter. These result in the greater extrusion effect between the cutter and the rock, which promotes the shear slip. Therefore, tensile damage and shear damage develop synchronously and ultimately lead to tensile–shear mixed failure.

4.3. Analysis of Cracks in Flank Side of the Cutter

Figure 9 shows the contour plots of cracks, maximum principal stress, and shear stress distribution on Section B. It can be seen that there is a high stress ahead of the ridged cutter

(Figure 9i). This can be contributed to the special "V" shape of the ridged cutter. During the cutting process, the convex ridge is the first spot that interacts with the rock. Then, a strong local load is generated at the ridge position. This will cause an increase in rock stress until it exceeds the strength of the rock and results in damage. This is accompanied by the development of radially distributed tensile and shear stress zones. As the cutter advances further, this zone, located on the flank side of the cutter, gradually expands. During this process, micro-cracks initiate and propagate toward the rock's surrounding surface, forming the macro-cracks (Figure 9e,f,i,j). It is worthy to note that two oblique cracks (at 45°) form in the distal region. However, as revealed in Reference [14], the conventional planar cutter squeezes the rock synchronously, and the maximum stress is located at the outer edge of the cutter. Thus, the rock fails owing to shear damage.

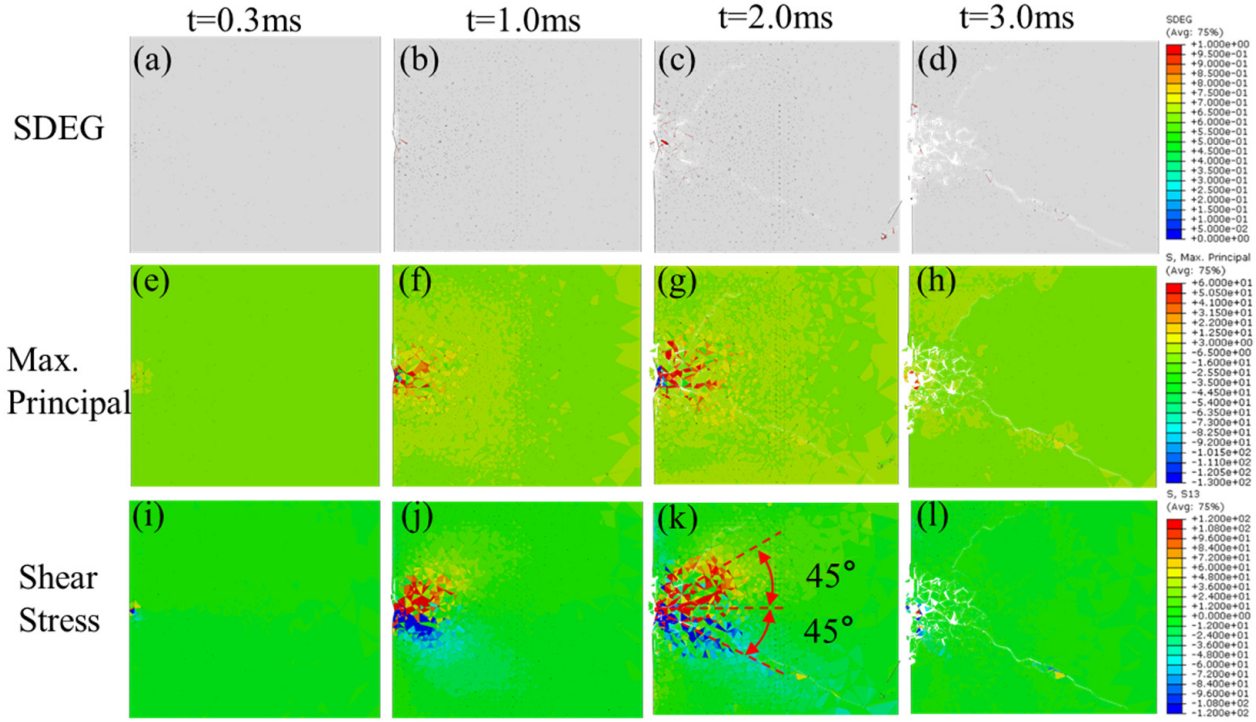


Figure 9. Characteristics of cracks on the flank side of the cutter (Section B).

As shown in Figure 10, six cohesive elements labeled B1 to B6 are selected along the flank crack, and their SDEG values are extracted at t = 2.0 ms, which are listed in Table 3. It can be seen that the normal SDEGs of B1 and B2 are greater than the shear SDEG, but none of them have reached the critical threshold of 0.9, especially the shear SDEG, which is zero. This means that these elements are currently in a tensile damage-dominated stage, and the change in shear SDEG is negligible. Element B3 has reached an SDEG value of 0.9 in both the normal and second tangential directions, indicating that tensile failure has already occurred at this location, while the shear crack has not yet fully developed. Elements B4 to B6 have reached the maximum SDEG value of 0.9 in all three directions, signifying that these elements have completely failed and the crack is fully interconnected.

Table 3. SDEG values of cohesive elements along the flank crack.

Location	Element Number	SDEG (n.s.t)
B1	122,949	(**0.81**, 0, 0)
B2	178,263	(**0.86**, 0, 0)
B3	183,816	(**0.90**, 0.19, **0.90**)

Table 3. *Cont.*

Location	Element Number	SDEG (n.s.t)
B4	92,743	(**0.90**, **0.90**, **0.90**)
B5	94,289	(**0.90**, **0.90**, **0.90**)
B6	134,529	(**0.90**, **0.90**, **0.90**)

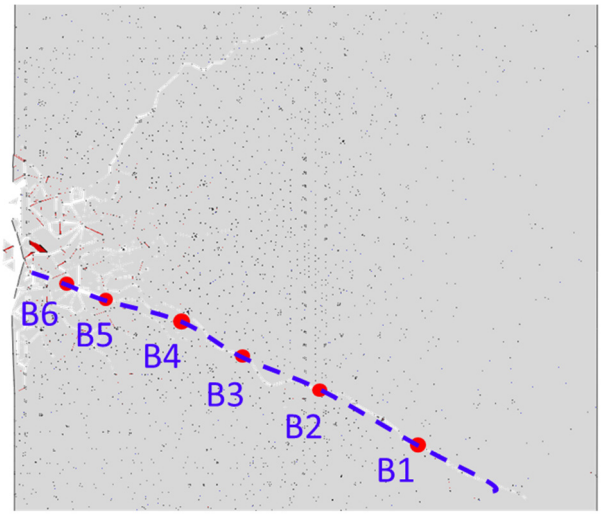


Figure 10. Locations of six elements along the crack on the flank side of the cutter (Section B).

The reasons for this behavior are similar to those for the cracks ahead of the cutter. Therefore, they are not repeated here. However, it is worth emphasizing that the oblique 45° crack can facilitate the release of the stress field within the rock, thereby promoting the spalling of larger rock chips.

4.4. Analysis of Sub-Cutter Cracks

The characteristics of cracks in the sub-cutter zone are also analyzed based on the information from Figure 7. In the initial stage, the rock below the cutter is under a complex compressive-shear stress state (Figure 7a,e). As the cutter gradually advances, a distinct tensile stress band forms in the sub-cutter zone (the red regions in Figure 7f,g). Meanwhile, due to the extrusion of the cutter, the rock ahead of the cutter moves forward while the sub-cutter rock remains relatively stationary. This relative motion between the two regions induces a shear stress band at the base of the cutter (Figure 7j,k). As the cutter continues to progress, the tensile and shear stress bands enlarge markedly and approximately reach a range of several times greater than the cutting depth. Notably, the sub-cutter crack propagates downward into the rock at an angle of approximately 25° (Figure 7c).

To quantify the damage evolution, six cohesive elements along the crack in the sub-cutter zone at t = 2.0 ms (Figure 11) are selected, and their SDEG values are listed in Table 4. The analysis shows that the normal SDEG of elements C1 and C2, though still below the critical threshold of 0.9, are higher than their shear SDEG. This indicates that the region is in a tensile damage-dominated crack initiation stage, with tensile damage being absolutely predominant. Elements C3 to C5 have reached a normal SDEG value of 0.9, while their shear SDEG remains below 0.9, suggesting that tensile failure has already occurred in this region, but shear failure has not yet fully developed. Only element C6, which is the closest to the cutter, has reached the critical threshold of 0.9 in all three directions. This demonstrates that element C6 has experienced both tensile and shear failure, and the crack at this location is fully propagated.

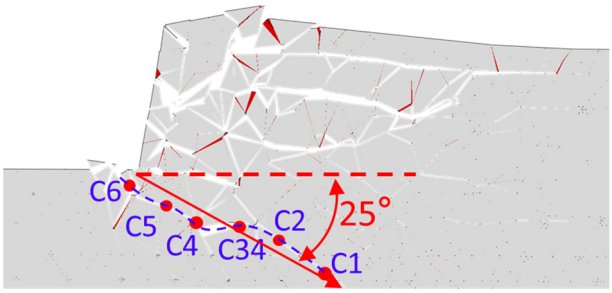


Figure 11. Locations of six elements along the crack in the sub-cutter zone (Section A).

Table 4. SDEG values of cohesive elements along the sub-cutter crack.

Location	Element Number	SDEG (n.s.t)
C1	103,827	(**0.68**, 0.50, 0.53)
C2	168,377	(**0.89**, 0.55, 0.58)
C3	89,598	(**0.90**, 0.83, 0.88)
C4	167,640	(**0.90**, 0.83, 0.84)
C5	190,704	(**0.90,** 0.77, 0.23)
C6	111,522	(**0.90**, **0.90**, **0.90**)

The damage distribution along the sub-cutter crack is consistent with that of the upward-concave crack ahead of the cutter. However, a greater number of elements (C1–C5) are influenced primarily by tensile damage, whereas only one element (C6) experiences combined tensile and shear damage. This pattern reveals that the sub-cutter rock is predominated by tensile failure, and only the rock close to the cutter experiences shear failure. Consequently, most of the sub-cutter region consists of tensile cracks, while only the region near the bottom of the cutter has mixed tensile–shear cracks.

5. Discussion

The SDEG data presented in this study reveal a common evolutionary sequence: that crack tips consistently exhibit significantly higher normal SDEG than the tangential components (i.e., A1–A3 in Table 2, B1–B2 in Table 3, and C1–C5 in Table 4). This indicates that micro-crack initiation begins with tensile damage. As the cracks develop and the applied load increases, the elements located closer to the rear of the crack path show synchronized growth in both normal and tangential SDEG until complete failure occurs (e.g., A4–A6 in Table 2, B3–B6 in Table 3, and C6 in Table 4). Such behavior indicates the subsequent involvement of shear damage, which acts in concert with tensile damage, ultimately leading to the macroscopic fracture.

This temporal sequence can be explained by fundamental principles of rock mechanics. Firstly, the tensile strength of rock is typically far lower than its shear strength (in this study, the tensile strength is 1.63 MPa, and the shear strength is 7.0 MPa, a difference of approximately 4.3 times). Consequently, in a complex stress field, once the locally derived tensile stress exceeds the tensile strength, micro-tensile cracks will initiate preferentially. This aligns with the phenomenon identified in this study, where crack tips always originate from tensile damage. As the tensile cracks open and the cutter moves forward, the preexisting cracks create geometric conditions which are condutive to shear slip. Meanwhile, the region at the rear of the crack experiences higher confining pressure because it is closer to the cutter. However, this high confining pressure significantly inhibits the propagation of tensile cracks but enhances the rock's shear strength to some extent, according to the M-C criterion [23]. Shear damage will therefore occur and dominate the failure only when

the shear stress is sufficient to overcome this enhanced shear strength. This results in the macroscopic observation of tensile initiation at the front of the crack, followed by shear propagation at the rear. This phenomenon is a universal law governed by the intrinsic strength properties of rock (low tensile strength, high shear strength) and the stress state transition during the failure process.

In addition to this common sequence, the crack patterns and macroscopic morphology also vary with the spatial location around the cutter, as summarized in Table 5. In the region ahead of the cutter, the extruding load from the ridged cutter serves as a core of stress transmission. Therefore, this region forms significant tensile stress bands (facilitating tension) and shear–stress bands (promoting shear), resulting in the final tensile–shear mixed failure mode. The orientation of the induced crack (at 45°) aligns with the direction of maximum shear stress. In contrast, the sub-cutter zone suffers the confinement of surrounding rocks. This confinement strongly suppresses the volume expansion caused by shear slip, making the development of shear damage difficult (except for the element C6, which is closest to the cutter). However, the extrusion from the cutter still generates sufficient tensile strain within the rock, inducing a dominant tensile stress which leads to a failure mode almost entirely controlled by tensile damage.

Table 5. A comparative analysis of crack patterns and their underlying causes across different regions.

Region	Element Number	Dominant Failure Mode (Based on SDEG)	Local Stress State Cause	Boundary and Loading Conditions
Ahead of cutter	Concave arc crack, 45° crack, horizontal crack	Tensile–shear mixed	Intersection of prominent tensile and shear stress bands	Free surface ahead; direct extrusion load from cutter
Sub cutter	Obliquely downward crack (at 25°)	Tensile-dominated	Prominent tensile stress band; weak shear stress band	High confinement; tensile deformation induced by direct extrusion
Cutter flank	Radially distributed, oblique cracks (at 45°)	Tensile initiation, mixed-mode propagation	Radial tensile stress field; complex stress from point load	Local point load effect of the ridge

In the flank-cutter zone, the distinctive geometry of the ridged cutter plays a decisive role. Its sharp ridge initiates a "wedging" effect, generating a radial tensile–shear stress field. The oblique cracks (at 45°) observed in this paper are therefore not simple shear fractures; rather, they are a mixed-mode failure combining both tensile and shear components. The cracks can efficiently release the rock stress and create favorable conditions for the subsequent coalescence of the concave cracks ahead of the cutter. This might ultimately enable the detachment of large rock fragments. This mechanism is one of the key reasons why the ridged cutter can generate a significantly larger volume fracture than the planar cutter.

In summary, the temporal uniformity of the crack evolution sequence during rock breaking by the ridged cutter reflects the intrinsic physical nature of rock failure, while the spatial diversity of crack patterns demonstrates the influence of external boundary conditions and local loading. The cracks ahead of the cutter result from the competition between shear and tensile failure induced by extrusion. The cracks below the cutter manifest the release of tensile deformation under high confining pressure. And the cracks on the cutter flank provide direct evidence of the "wedging" effect caused by the unique geometry of the ridged cutter.

6. Conclusions

In order to clarify the unclear evolution mechanism of cracks around the ridged cutter, this paper established a three-dimensional finite element model of dynamic rock

breaking with the ridged cutter, based on the Finite–Discrete Element Method (FDEM), and systematically investigated the characteristic of crack evolution during the rock-breaking process. The main conclusions are as follows:

(1) The ridged cutter breaks rock primarily through a combination of tension and shear, distinct from the shear-based mechanism of conventional planar cutters.
(2) The rock-breaking proceeds through three stages: compaction, micro-failure, and volumetric fragmentation, with damage patterns exhibiting regional heterogeneity.
(3) Crack evolution follows a consistent "tension-initiated and shear-propagated" sequence. Tensile damage initiates first at crack fronts due to stress concentration, while shear damage subsequently develops at the rear under high shear stress, culminating in mixed macro-cracks.
(4) The spatial distribution of cracks is highly heterogeneous. The zone ahead of the cutter contains mixed tensile–shear cracks, forming upward-concave, horizontal, and 45° oblique cracks. The sub-cutter zone is dominated by tensile cracks. The flank zone features a radial stress field accompanied by oblique 45° cracks.

This study systematically analyzes the crack evolution process during rock fragmentation by the ridged cutter, addressing the current gap regarding crack propagation sequences and failure modes. The findings provide clear guidance for the design of non-planar cutters, such as optimizing geometry parameters to regulate radial stress fields and crack propagation with the aim of maximizing rock fragmentation efficiency. Future research should further consider the influence of complex environmental factors such as confining pressure, drilling fluid, and temperature. Despite the insightful findings, it is important to note that this study employed a constant friction coefficient (0.4) at the cutter-rock interface, the sensitivity of which was not exhaustively analyzed. Future work will involve a systematic parametric study to quantitatively assess the influence of the friction coefficient and other interfacial properties on the rock fragmentation process, as well as quantitative data on cracks. The present FDEM model requires significant computational time, particularly in large-scale simulations where computational efficiency is limited. Future work may incorporate parallel computing (e.g., MPI/GPU acceleration) and adaptive mesh refinement to improve the efficiency and refine the depiction of the rock fragmentation process.

Author Contributions: Conceptualization, J.L. and C.D.; methodology, J.L.; software, T.H.; validation, J.L. and C.D.; formal analysis, J.L.; investigation, C.D.; resources, X.M.; data curation, J.L.; writing—original draft preparation, T.H.; writing—review and editing, J.L.; visualization, C.M.; supervision, J.L.; project administration, J.L.; funding acquisition, J.L. All authors have read and agreed to the published version of the manuscript.

Funding: This research was funded by the Science and Technology Research Program of Chongqing Municipal Education Commission (Grant No. KJQN202101518, No. KJQN202401506) and the Open Fund (OGE202303-14) of Key Laboratory of Oil & Gas Equipment, Ministry of Education (Southwest Petroleum University).

Data Availability Statement: The original contributions presented in this study are included in the article. Further inquiries can be directed to the corresponding author.

Conflicts of Interest: The authors declare no conflicts of interest.

References

1. He, D.F.; Jia, C.Z.; Zhao, W.Z.; Xu, F.Y.; Luo, X.R.; Liu, W.H.; Tang, Y.; Gao, S.L.; Zheng, X.J.; Li, D.; et al. Research progress and key issues of ultra-deep oil and gas exploration in China. *Pet. Explor. Dev.* **2023**, *50*, 1333–1344. [CrossRef]
2. Hussein, A.; Al-Anezi, N.; Al-Sarraf, A.; Akshaya, K.; Hussain, A.; Harish, M.; Osama, G.; Zhang, Y. Thermally Stable Cutter Technology Advances PDC Performance in Hard and Abrasive Formations. In Proceedings of the IPTC 2013: International Petroleum Technology Conference, Beijing, China, 26–28 March 2013. [CrossRef]

3. Clegg, J. Faster, Longer, and More Reliable Bit Runs With New-Generation Thermostable PDC Cutter. In Proceedings of the SPE Annual Technical Conference and Exhibition, San Antonio, TX, USA, 24–27 September 2006. [CrossRef]
4. Zou, D.; Pan, L.; Cui, Y.; Xu, J. Rock Breaking Mechanism and Experimental Study of Axe-shaped PDC Cutter. *Chin. Pet. Mach.* **2022**, *50*, 34–40. [CrossRef]
5. Xu, W.; Shi, H.; Cao, Q.; Shi, X.; Hu, X.; Xiong, C.; Chen, H. Experimental Study on Conglomerate Breaking Characteristic of Conical PDC cutter. *Chin. Pet. Mach.* **2021**, *49*, 9–16. [CrossRef]
6. Xiong, C.; Huang, Z.; Shi, H.; Yang, R.; Wu, G.; Chen, H.; He, W. Performances of a stinger PDC cutter breaking granite: Cutting force and mechanical specific energy in single cutter tests. *Pet. Sci.* **2023**, *20*, 1087–1103. [CrossRef]
7. Fu, X.; Huang, Z.; Shi, H.; Song, H.; Wu, H. Comparison of fracture characteristics of different PDC cutters penetrating carbonate rock. *Geoenergy Sci. Eng.* **2023**, *223*, 211536. [CrossRef]
8. Shao, F.; Liu, W.; Gao, D. Effects of the chamfer and materials on performance of PDC cutters. *J. Pet. Sci. Eng.* **2021**, *205*, 108887. [CrossRef]
9. Zhang, M. Simulation of PDC Bit Rock Breaking Based on Discrete Element Method. Master's Thesis, Southwest Petroleum University, Chengdu, China, 2017.
10. Yao, J.L.; Liu, B. Discrete element study on rock failure mechanism by shaped PDC cutter under formation conditions with in-situ stress and temperature. In Proceedings of the International Geomechanics Symposium, Abu Dhabi, United Arab Emirates, 7–9 November 2022. [CrossRef]
11. Kuang, Y.C.; Peng, Y.Z.; Zhang, Y. Numerical Simulation and Experiment on Rock Breaking of PDC Bits. *Chin. Pet. Mach.* **2015**, *43*, 10–13. [CrossRef]
12. Gao, M.Y.; Zhang, K.; Zhou, Q.; Zhou, Y.F.; Liu, B. Research on PDC High Speed Rock Cutting Mechanism Based on ABAQUS. *Chin. Pet. Mach.* **2019**, *47*, 471–477. [CrossRef]
13. Zhu, X.H.; Li, H. Numerical Simulation on Mechanical Special Energy of PDC Cutter Rock-cutting. *J. Basic Sci. Eng.* **2015**, *23*, 182–191. [CrossRef]
14. Liu, J.X.; Zheng, H.L.; Kuang, Y.C.; Xie, H.; Qin, C. 3D numerical simulation of rock cutting of an innovative non-planar face PDC cutter and experimental verification. *Appl. Sci.* **2019**, *9*, 4372. [CrossRef]
15. Chen, H.D.; Liu, H.M.; Han, X.; Jin, Y.; Liang, J.W.; Wang, S.G.; Lu, Y.H. Study on Rock Breaking Mechanism and Optimization of PDC Cutter for Deep Water HTHP Plastic Mudstone. In Proceedings of the ARMA U.S. Rock Mechanics/Geomechanics Symposium, Santa Fe, NM, USA, 26–29 June 2022. [CrossRef]
16. Shao, F.Y.; Liu, W.; Gao, D.L.; Ye, Y.C. Study on rock-breaking mechanism of axe-shaped PDC cutter. *J. Pet. Sci. Eng.* **2021**, *205*, 108922. [CrossRef]
17. Qin, C.S.; Sun, H.B.; Li, L.P.; Liu, X.G.; Liu, Z.H.; Feng, C.; Sun, Z.Z. Continuous and discontinuous numerical simulation of the breaking process for PDC cutter under composite impact loading. *Coal Geol. Explor.* **2025**, *51*, 109–120. [CrossRef]
18. Liu, Y.; Wu, Z.J.; Chu, Z.F.; Weng, L.; Xu, X.Y.; Zhou, Y.; Gao, B.; Mao, C.G. Rock breaking mechanism with mechanical impact under confining pressure based on FDEM. *J. Cent. South Univ. Sci. Technol.* **2023**, *54*, 866–879. [CrossRef]
19. Wu, Z.J.; Zhang, P.L.; Liu, Q.S.; Li, W.F.; Jiang, H.Z. Dynamic failure analysis of reinforced concrete slab based on cohesive element under explosive load. *Eng. Mech.* **2018**, *35*, 79–90. [CrossRef]
20. Feng, C.; Li, S.H.; Zheng, B.X.; Cui, X.R.; Jia, J.J. Numerical simulation on complete process of three-dimensional bench blasting in an open-pit mine based on CDEM. *Explos. Shock Waves* **2019**, *39*, 110–120. [CrossRef]
21. Munjiza, A. *The Combined Finite-Discrete Element Method*; John Wiley & Sons: New York, NY, USA, 2004.
22. Li, P.T.; Liu, Q.S. Investigation of tunnel excavation numerical analysis method for the combined finite-discrete element method. *Eng. Anal. Bound. Elem.* **2024**, *165*, 105779. [CrossRef]
23. Wu, S.C.; Li, L.P.; Zhang, X.P. *Rock Mechanics*; Higher Education Press: Beijing, China, 2021.
24. Huang, A.L.; Guo, W.; Zou, Y.; Zou, J.W.; Deng, R.; Ye, B.L. Numerical simulation of rock breaking by PDC cutter with finite-discrete-infinite element method. *Geoenergy Sci. Eng.* **2023**, *225*, 211725. [CrossRef]
25. Du, C.L.; Liu, Q.S.; Lei, Y.M.; Liu, H.; Bo, Y. The Calibration of Microscopic Parameters for the 3D Finite-Discrete Element Method. *Rock Mech. Rock Eng.* **2024**, *57*, 2195–2212. [CrossRef]
26. Zhao, H. Experimental and Simulation Research on Rock-Breaking Mechanism of Axe-Shaped PDC Cutter. Master's Thesis, China University of Petroleum (Beijing), Beijing, China, 2023.
27. Shao, L.T.; Li, M.; Ding, M.L. Study on the Mechanical Model of Slag and Quasi-Static Analysis of Slag Samples in the Radiant Syngas Cooler. *Asia-Pac. J. Chem. Eng.* **2025**, e70066. [CrossRef]
28. Zhou, G.T.; Xu, Z.L. 3D mesoscale investigation on the compressive fracture of concrete with different aggregate shapes and interface transition zones. *Constr. Build. Mater.* **2023**, *393*, 132111. [CrossRef]
29. Naderi, S.; Tu, W.L.; Zhang, M.Z. Meso-Scale Modelling of Compressive Fracture in Concrete with Irregularly Shaped Aggregates. *Constr. Build. Mater.* **2021**, *140*, 106317. [CrossRef]

30. Liu, Z.H.; Kong, C.Y.; Lv, R.; Ma, Z.K.; Wei, C.Y. Characteristic of rock breaking by a saw blade-impact hammer combination cutterhead. *J. Vib. Shock* **2024**, *43*, 301–311. [CrossRef]
31. Liu, Z.H.; Lv, R.; Zheng, Y.L.; Ma, Z.G.; Liu, K.; Wei, C.Y. Experimental and Numerical Investigation of Rock Breaking Performance by Single Impact Hammer Under Saw Blade Pre-slotted Conditions. *Rock Mech. Rock Eng.* **2025**, *58*, 3501–3521. [CrossRef]
32. Gao, W.; Liu, X.; Hu, J.; Feng, Y.T. A novel bilinear constitutive law for cohesive elements to model the fracture of pressure-dependent rocks. *Rock Mech. Rock Eng.* **2022**, *55*, 521–540. [CrossRef]
33. Yang, R.S.; Kang, Y.Q.; Yang, L.Y.; Liu, K.; Ding, C.X.; Fan, J.H. Influence of the postion and depth of pre-cutting kerfs on the rock breaking by SBM cutter. *J. China Coal Soc.* **2024**, *49*, 415–425. [CrossRef]
34. Guan, Z.C.; Hu, H.G.; Wang, B.; Sun, M.W.; Liu, Y.W.; Xu, Y.Q. Experimental study on rock-breaking efficiency of PDC bit based on mechanical specific energy and sliding frictional coefficient. *J. China Univ. Pet. Nat. Sci. Ed.* **2019**, *43*, 92–100. [CrossRef]
35. Yang, X.W.; Xiang, J.S.; Latham, J.P.; Naderi, S.; Wang, Y.H. Cracking and fragmentation in percussive drilling: Insight from FDEM simulation. *J. Rock Mech. Geotech. Eng.* **2025**. [CrossRef]

Disclaimer/Publisher's Note: The statements, opinions and data contained in all publications are solely those of the individual author(s) and contributor(s) and not of MDPI and/or the editor(s). MDPI and/or the editor(s) disclaim responsibility for any injury to people or property resulting from any ideas, methods, instructions or products referred to in the content.